Journal of Energy Chemistry 76 (2023) 547–556

Contents lists available at ScienceDirect

Journal of Energy Chemistry

journal homepage: www.elsevier.com/locate/jechem

http://www.journals.elsevier.com/journal-of-energy-chemistry/

Achieving high-capacity and long-life K^+ storage enabled by constructing yolk-shell Sb_2S_3@N, S-doped carbon nanorod anodes

Bensheng Xiao [a,1], Hehe Zhang [a,1], Zhefei Sun [a], Miao Li [a], Yingzhu Fan [e], Haichen Lin [c], Haodong Liu [c], Bing Jiang [d], Yanbin Shen [e], Ming-Sheng Wang [a], Meicheng Li [d], Qiaobao Zhang [a,b,*]

[a] Department of Materials Science and Engineering, College of Materials, Xiamen University, Xiamen 361005, Fujian, China
[b] Fujian Key Laboratory of Surface and Interface Engineering for High Performance Materials (Xiamen University), Xiamen 361005, Fujian, China
[c] Department of Nanoengineering, University of California San Diego, La Jolla, CA, 92093, United States
[d] State Key Laboratory of Alternate Electrical Power System with Renewable Energy Sources, School of New Energy, North China Electric Power University, Beijing 102206, China
[e] i-Lab, CAS Center for Excellence in Nanoscience, Suzhou Institute of Nano-Tech and Nano-Bionics (SINANO), Chinese Academy of Sciences, Suzhou 215123, Jiangsu, China

ARTICLE INFO

Article history:
Received 21 September 2022
Revised 30 September 2022
Accepted 30 September 2022
Available online 8 October 2022

Keywords:
Antimony sulfide
Yolk-shell structure
In situ TEM
Potassium-ion batteries
Super-stable cyclability

ABSTRACT

As promising anode candidates for potassium-ion batteries (PIBs), antimony sulfide (Sb_2S_3) possesses high specific capacity but suffers from massive volume expansion and sluggish kinetics due to the large K^+ insertion, resulting in inferior cycling and rate performance. To address these challenges, a yolk-shell structured Sb_2S_3 confined in N, S co-doped hollow carbon nanorod (YS-Sb_2S_3@NSC) working as a viable anode for PIBs is proposed. As directly verified by in situ transmission electron microscopy (TEM), the buffer space between the Sb_2S_3 core and thin carbon shell can effectively accommodate the large expansion stress of Sb_2S_3 without cracking the shell and the carbon shell can accelerate electron transport and K^+ diffusion, which plays a significant role in reinforcing the structural stability and facilitating charge transfer. As a result, the YS-Sb_2S_3@NSC electrode delivers a high reversible K^+ storage capacity of 594.58 mA h g^{-1} at 0.1 A g^{-1} and a long cycle life with a slight capacity degradation (0.01% per cycle) for 2000 cycles at 1 A g^{-1} while maintaining outstanding rate capability. Importantly, utilizing in in situ/ex situ microscopic and spectroscopic characterizations, the origins of performance enhancement and K^+ storage mechanism of Sb_2S_3 were clearly elucidated. This work provides valuable insights into the rational design of high-performance and durable transition metal sulfides-based anodes for PIBs.

1. Introduction

Potassium-ion batteries (PIBs) have been regarded as one of the most promising next-generation energy storage systems because of their low cost, abundant sources, and low redox potential (K^+/K: −2.93 V vs. standard hydrogen electrode) [1–6]. However, due to the large size of K^+ (1.38 Å vs. 0.76 Å for Li^+), traditional materials would undergo massive volume changes and sluggish potassiation kinetics upon potassiation/depotassiation, resulting in rapid capacity decay and low reversibility of K^+ storage [7,8]. For example, the commercial graphite electrode, which exhibited a volume expansion of ∼61% after full potassiation and a capacity loss of 49% after only 50 cycles, was far from satisfactory in PIBs [9]. Therefore, to meet the requirements for practical applications of PIBs, it is of great significance, yet quite challenging to design and construct anode materials with high K^+ storage capacity and stable cyclability.

Antimony (Sb)-based materials, including metallic Sb, intermetallic Sb alloys, and Sb chalcogenides, have been widely investigated in energy-storage devices owing to their high theoretical capacities [10–14]. Among them, Sb_2S_3 has drawn extensive attention as it proceeds a conversion-alloy reaction with a higher reversible theoretical capacity and better mechanical stability than metallic Sb [15,16]. Nevertheless, Sb_2S_3 working as an anode for PIBs still suffers from several drawbacks, such as poor intrinsic electrical conductivity and severe volume expansion (∼393%), resulting in limited ion/charge transfer and fast capacity fading [17,18]. To alleviate these problems, extensive studies have attempted to engineer nanostructures, build coating layers, design morphology, etc [17,19–21]. Among these strategies, carbon coating has proven indispensable for improving electronic conductivity, preventing the aggregation of Sb_2S_3, and inhibiting

* Corresponding author.
E-mail address: zhangqiaobao@xmu.edu.cn (Q. Zhang).
[1] These authors contributed equally to this work.

https://doi.org/10.1016/j.jechem.2022.09.050

polysulfide shuttling, thereby mitigating electrode failure [3,22]. However, Cheng's work revealed that the structural stability of Sb_2S_3 could only be improved to a limited extent by surface coating since its enormous expansion stress would destroy the carbon layers during cycling [16]. In this regard, it is necessary to construct buffer space between the Sb_2S_3 materials and coating layers, i.e., yolk-shell structures, where the volume expansion can be effectively accommodated and thus reinforce the structural stability. However, the yolk-shell Sb_2S_3@C structures working as anodes in PIBs are rarely reported. And, the effects of carbon coating and buffer space on electrochemically induced structural evolution governing enhanced performance remain elusive and are need to be further clarified.

To this end, a yolk-shell structured Sb_2S_3 confined in N, S co-doped hollow carbon nanorod (YS-Sb_2S_3@NSC) was synthesized through a facile template-free strategy and further investigated as reliable anode for PIBs. In particular, utilizing in situ transmission electron microscopy (TEM), the structural evolution of bare Sb_2S_3, core-shell structured Sb_2S_3@NSC (CS-Sb_2S_3@NSC), and YS-Sb_2S_3@NSC upon potassiation was systematically investigated, which manifested the crucial role of surface layer cooperated with buffer space in the mechanical stability and K^+ transfer kinetics of Sb_2S_3-carbon composites. In our case, the N, S-doped carbon shells are conducive to providing effective electron/K^+ transfer pathways, while the inner cavity can effectively accommodate the enormous expansion stress of active Sb_2S_3, thus boosting the rate and cycling performance. By integrating X-ray photoelectron spectroscopy (XPS) with time-of-flight secondary ion mass spectrometry (TOF-SIMS) measurements, we reveal the formation of the F-rich solid electrolyte interface (SEI) on YS-Sb_2S_3@NSC, favoring for reducing the solubility of inorganic substances in the electrolyte and stabilizing the interface, and thus accounting for enhanced rate performance. Accordingly, the as-obtained YS-Sb_2S_3@NSC demonstrates superior K^+ storage performance, namely, high reversible capacity, outstanding rate capability and cycling stability, outperforming bare Sb_2S_3, CS-Sb_2S_3@NSC and reported results of Sb-based anodes. This work provides insights into the rational design of high-performance transition metal sulfides-based anodes for advanced PIBs.

2. Experimental

2.1. Sample preparation

2.1.1. Synthesis of bare Sb_2S_3 nanorods

In a typical process, 0.92 g of $SbCl_3$, 0.97 g of L-cysteine, and 1.9 g of $Na_2S{\cdot}9H_2O$ were dissolved in 80 mL of deionized water in turn and subsequently stirred for 3 h to form a uniform dark yellow suspension. Then, the mixture was transferred to a 100 ml hydrothermal kettle and heated to 180 °C for 12 h. After that, the cooled powder was repeatedly washed with ethanol and deionized water by suction filtration. Finally, the target product was collected after drying at 60 °C for 12 h.

2.1.2. Synthesis of YS-Sb_2S_3@NSC nanorods and CS-Sb_2S_3@NSC nanorods.

First, 90 mg of bare Sb_2S_3 nanorods was added to 300 mL of Tris-buffer solution (10 mM) with 1 h of ultrasonic dispersion, and then 120 mg of dopamine was added and stirred for 6 h. After washing with deionized water and ethanol using suction filtration, and drying at 60 °C overnight, Sb_2S_3@PDA nanorods were collected. For YS-Sb_2S_3@NSC nanorods, the obtained Sb_2S_3@PDA was placed in a porcelain boat and heated at 500 °C for 1.5 h under the N_2 atmosphere with a heating rate of 3 °C min^{-1}. For CS-Sb_2S_3@NSC nanorods, Sb_2S_3@PDA was heated at 500 °C for 0.5 h under the same conditions.

2.2. Materials characterization

The synthesized samples' morphology and structure were characterized by scanning electron microscopy (SEM) (Zeiss SIGMA) and TEM (FEI Talos F200s). The crystal structure information was obtained by X-ray diffraction (Cu $K_{\alpha 1}$ source, λ = 1.5418 Å). X-ray photoelectron spectroscopy (XPS) was investigated through an EscaLab Xispec trometer using Al *K* Alpha radiation. The Brunauer-Emmett-Teller (BET) analysis was carried out by a Micromeritics 3FLEX analyzer. The thermogravimetric analysis (TGA) was performed on a NETZSCH STA 2500 under O_2 atmosphere from 25 to 800 °C with a heating rate of 10 °C min^{-1}. Raman spectra were collected by a Horiba Scientific LabRAM HR-Evolution.

2.3. Electrochemical characterization

For the preparation of working electrodes, the active materials, Super P and carboxymethyl cellulose were mixed in water with a weight ratio of 8:1:1 to form a homogeneous slurry. The slurry was then coated on the copper foil, and the diameter of the electrodes was cast into 12 mm. CR2016 coin-type cells were assembled in a high Ar-filled glove box, which consisted of metallic K foils as the counter electrode, glass fibers as the separator, and 5 M KFSI in DME solution as the electrolyte. And, the mass loadings of the anode active materials were measured to be 1.0–1.1 mg cm^{-2}. The capacity of CS-Sb_2S_3@NC and YS-Sb_2S_3@NSC was calculated based on their whole mass. The galvanostatic discharge/charge profiles were tested on a Neware CT-3008 W with a voltage window of 0.01–3 V at 30 °C. The cyclic voltammetry (CV) and electrochemical impedance spectroscopy (EIS, frequency range from 0.01 Hz to 100 KHz and the charging and discharging process exerts current density was 0.1 A g^{-1}). Galvanostatic intermittent titration technique (GITT) was tested on a Land battery-testing system. A TOF-SIMS (TOF.SIMS5-100) was used for the depth analysis of the chemical composition of the anodes. A Cs^+ ion beam (500 eV, 20 nA) was used for depth profiling analysis (200 μm × 200 μm, 1200 s). The analysis area is 50 μm × 50 μm. For electrode after-cycling characterizations, coin cells were dissembled in the glove box and washed with DME for 30 min to remove residual potassium salts.

2.4. In situ TEM observation

The dynamic potassiation processes were observed by an FEI Talos-F200s TEM using a Nanofactory TEM-STM holder at 200 kV. Sb_2S_3-based nanorods were loaded on a Mo tip as the working electrode, while K metal attached on a Cu tip was used as the counter electrode. The K_2O on the surface of the K metal acted as the solid electrolyte. A positive bias of 3 V was applied on the Cu tip to initiate the potassiation process.

3. Results and discussion

3.1. Preparation and structural properties

The preparation process of YS-Sb_2S_3@NSC is illustrated in Fig. 1 (a). First, Sb_2S_3 nanorods were prepared by a simple hydrothermal reaction. Subsequently, the nanorods were coated with PDA to form a core-shell structured Sb_2S_3@PDA. Then, the Sb_2S_3@PDA nanorods were treated at 500 °C for 1.5 h under the N_2 atmosphere, accompanied by partial volatilization of Sb_2S_3, eventually forming

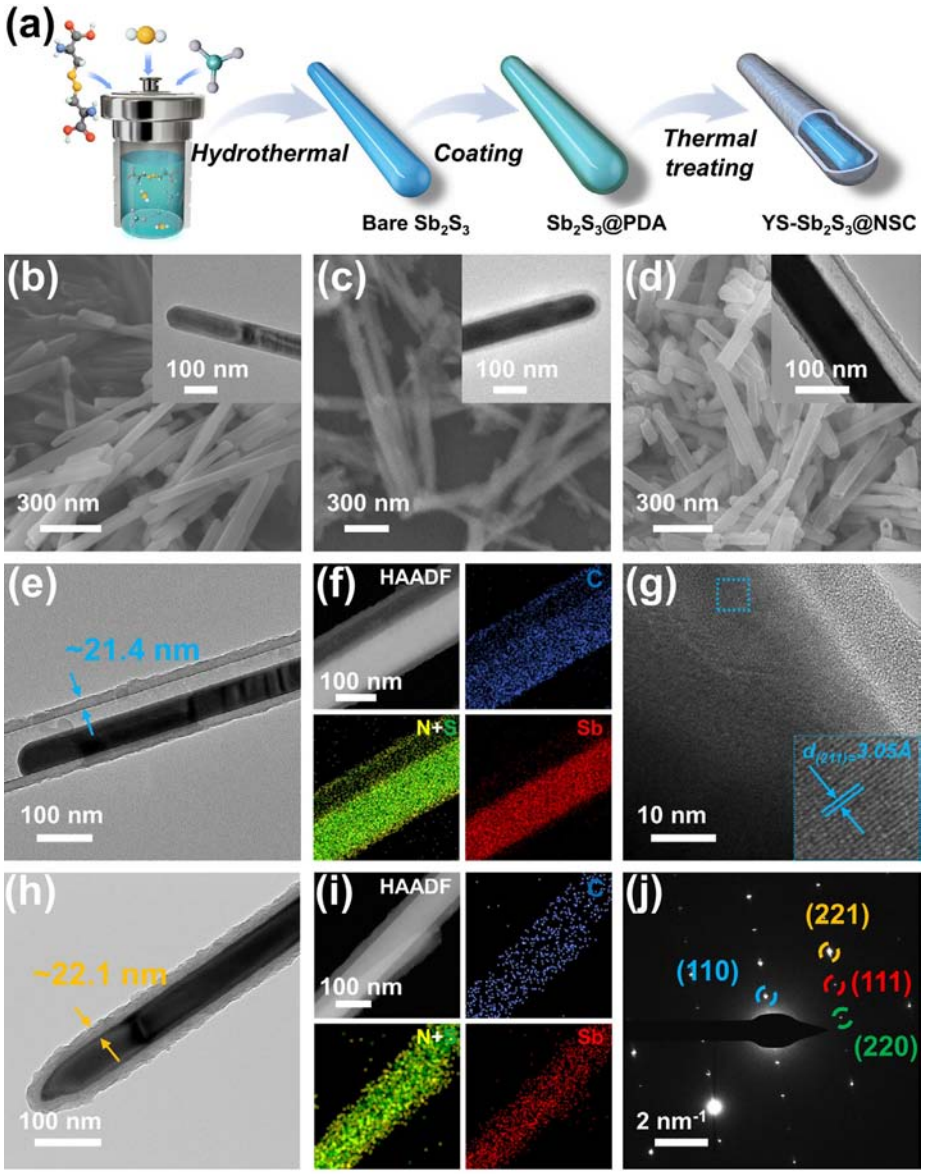

Fig. 1. (a) Illustration of preparation of YS-Sb_2S_3@NSC. (b–d) SEM and inset TEM images of Sb_2S_3, Sb_2S_3@PDA, and YS-Sb_2S_3@NSC. (e) TEM, (f) EDS mapping, (g) HRTEM, and (j) corresponding SAED pattern images of YS-Sb_2S_3@NSC. (h, i) TEM and EDS mapping images of CS-Sb_2S_3@NSC.

the yolk-shell structured Sb_2S_3@NSC. The core-shell structured Sb_2S_3@NSC was synthesized through heating Sb_2S_3@PDA at 500 °C for 0.5 h.

The morphology and structure of the above Sb_2S_3-based material captured by SEM and TEM are shown in Fig. 1 and Figs. S1–S4. Further prolonging the heating duration to 2.5 h at 500 °C cause the complete disappearance of Sb_2S_3 forming hollow NSC (Fig. S5). The effects of the heat treatment temperature and rate on the morphology and structure of Sb_2S_3-based materials are provided in Figs. S6–S9 with the corresponding electrochemical performance shown in Fig. S10. Fig. 1(b–d) displays the structural evolution of Sb_2S_3 materials during the synthetic process, consistent with the schematic illustration in Fig. 1(a). Apparently, after the annealing process (Fig. 1d and e), the rod-like morphology remains well, and the interior void space between the Sb_2S_3 core and carbon shell can be clearly observed, manifesting the successful formation of a yolk-shell Sb_2S_3@NSC structure. For comparison, as displayed in Fig. 1(h), the core-shell structured Sb_2S_3@NSC (CS-Sb_2S_3@NSC) was also prepared, where the 22.1 nm-thick amorphous carbon shell tightly wraps the Sb_2S_3 nanorods without any interior space. Energy dispersive spectroscopy (EDS) mapping images in Fig. 1(f and i) further demonstrate the structural difference between YS-Sb_2S_3@NSC and CS-Sb_2S_3@NSC, and confirm the co-doping of N and S elements in the carbon shell. The high-resolution TEM (HRTEM) image of YS-Sb_2S_3@NSC is given in Fig. 1(g), in which the lattice fringe spacings of 3.05 Å correspond to the (211) plane of Sb_2S_3 [23]. The selected area electron diffraction (SAED) pattern in Fig. 1(j) indicates the single crystalline nature of the as-prepared Sb_2S_3-based materials.

Fig. 2(a) shows the X-ray diffraction (XRD) patterns of all samples, where their diffraction peaks match well with the standard card of the orthorhombic Sb_2S_3 (JCPDS Card No. 42-1393), following HRTEM and SAED results. Raman spectra can further investigate the structural characteristics. As seen in Fig. 2(b), the peak located at 278 cm^{-1} corresponds to the vibrations of pyramidal units Sb–S in Sb_2S_3 [24]. Distinct from bare Sb_2S_3, two broad peaks at about 1340 and 1590 cm^{-1} appear in CS-Sb_2S_3@NSC and YS-Sb_2S_3@NSC, which stand for the D band and G band of the carbon shell [25], respectively, thus indicating the successful carbon coating in the latter two samples. The N_2 absorption/desorption analy-

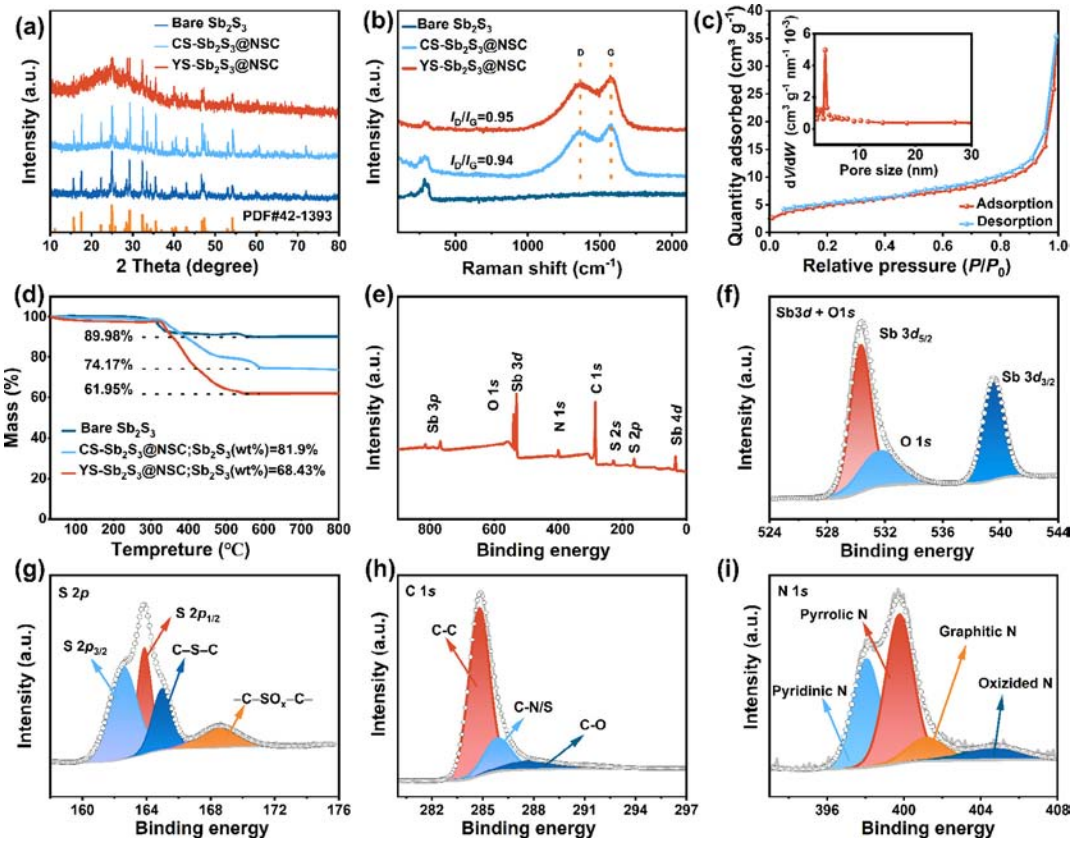

Fig. 2. (a) XRD patterns and (b) Raman spectra of the three samples. (c) N_2 adsorption/desorption isotherms and pore-size distribution (inset), (d) TGA curve, (e) XPS spectra, and (f–i) high-resolution XPS spectra images of Sb 3*d*, S 2*p*, C 1*s* and N 1*s* for YS-Sb_2S_3@NSC.

sis is performed in Fig. 2(c) and Fig. S11 with the information of specific surface area and the corresponding pore size shown in Table S1. Compared with bare Sb_2S_3, CS-Sb_2S_3@NSC and YS-Sb_2S_3@NSC possess a larger surface area with a pore distribution centered at about 4 nm, which results from the abundant mesopores in the carbon shells. According to thermal gravimetric analyzer (TGA) tests (Fig. 2d, the detailed calculation process and product analysis are shown in Fig. S12), the Sb_2S_3 contents of CS-Sb_2S_3@NSC and YS-Sb_2S_3@NSC are calculated to be 81.9 and 68.43 wt%, respectively. The high Sb_2S_3 content guarantees a high theoretical capacity. The components and valence bonds of YS-Sb_2S_3@NSC were revealed by XPS analysis. The survey spectrum in Fig. 2(e) demonstrates the presence of Sb, S, C, N, and O elements. As shown in Fig. 2(f), the high-resolution Sb 3*d* and O 1*s* XPS spectra overlap. Two pronounced peaks centered at 530.28 and 539.58 eV can be ascribed to Sb $3d_{5/2}$ and Sb $3d_{3/2}$, respectively [26], while the peak at 531.68 eV belongs to O 1*s*. As for S 2*p* (Fig. 2g), the fitted peaks at 162.38, 163.8, 164.98, and 168.58 eV can be assigned to S $2p_{3/2}$, S $2p_{1/2}$, C–S–C, and C–SO_x–C, respectively, in good agreement with previous reports [27]. In the N 1*s* spectrum (Fig. 2i), the high contents of pyridinic N and pyrrolic could effectively promote the K^+-adsorption ability [3].

3.2. Potassium-ion storage performance

The potassium-ion storage properties of bare Sb_2S_3, CS-Sb_2S_3@NSC, and YS-Sb_2S_3@NSC electrodes were investigated in Fig. 3. Fig. 3(a) shows the CV curves of YS-Sb_2S_3@NSC at 0.1 mV s^{-1}. The irreversible cathodic peak at around 0.7 V in the first cycle can be attributed to the formation of a SEI layer [17], as verified by the below XPS and TOF-SIMS measurements. In the following scans, the essentially unchanged curves demonstrate the good electrochemical reversibility of YS-Sb_2S_3@NSC. In addition, the cathodic peak centered at 1.32 V stands for the conversion process of Sb_2S_3 to Sb, while the subsequent two peaks at 0.54 and 0.06 V are ascribed to the two-step alloying process to form K_3Sb [16,28]. During the depotassiation process, two anodic peaks at 0.66 and 1.23 V correspond to the dealloying and deconversion processes to reform Sb_2S_3 [29]. The galvanostatic discharge-charge curves of YS-Sb_2S_3@NSC at different cycles are shown in Fig. 3(b). Calculated from the first discharge and charge capacities (767.7 and 483.76 mA h g^{-1}), the initial coulombic efficiency (ICE) is 63%. The voltage profiles from the 10th cycle almost overlap (Fig. 3b), demonstrating the structural stability of YS-Sb_2S_3@NSC electrodes. The cycling performance of YS-Sb_2S_3@NSC and the other two samples at 0.1 A g^{-1} is depicted in Fig. 3(c). Despite the fact that the CS-Sb_2S_3@NSC electrode outperforms bare Sb_2S_3, however, only a low capacity of 281 mA h g^{-1} can be remained for CS-Sb_2S_3@NSC after 75 cycles, revealing that the surface coating is not robust enough to restrain the volume fluctuation of Sb_2S_3. Instead, the YS-Sb_2S_3@NSC electrode exhibits excellent cycling stability, which maintains a high reversible capacity of 594.58 mA h g^{-1} after 100 cycles with almost no capacity decay. These results suggest the importance of the surface layer cooperating with buffer space in stabilizing the Sb_2S_3 materials. The phenomenon of capacity rise after about 10 cycles of CS-Sb_2S_3@NSC and YS-Sb_2S_3@NSC may result from the morphological reorganization of the materials as well as the optimization and stabilization of SEI during cycling [26,30].

The rate capability of the three electrodes was displayed in Fig. 3(d). The YS-Sb_2S_3@NSC electrode exhibits the best rate performance, delivering high reversible capacities of 629, 579, 547.7,

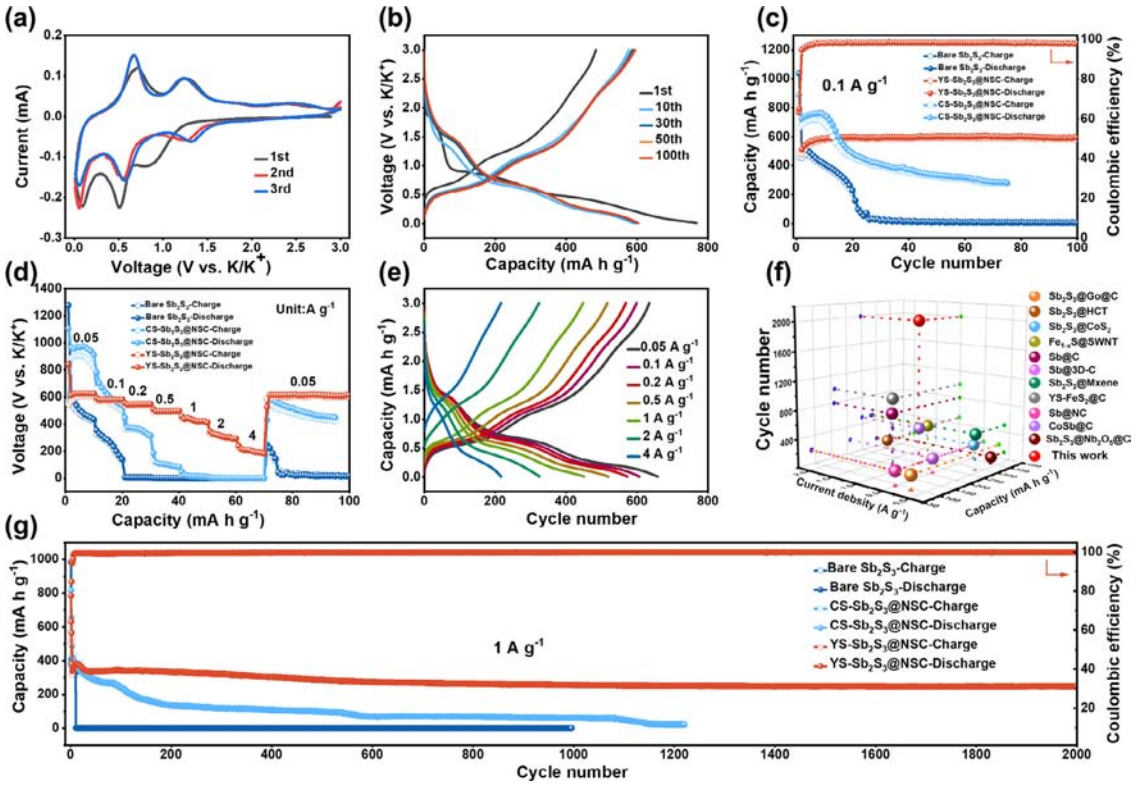

Fig. 3. (a) CV curves of YS-Sb_2S_3@NSC at 0.1 mV s^{-1}. (b) Discharge-charge curves of YS-Sb_2S_3@NSC at 0.1 A g^{-1}. (c) Cycle performance of the three electrodes at 0.1 A g^{-1}. (d) Rate performance of the three electrodes. (e) Discharge-charge profiles of YS-Sb_2S_3@NSC at various current densities. (f) Comparison between YS-Sb_2S_3@NSC and other reported Sb-based materials. (g) Cycling performance of bare Sb_2S_3, CS-Sb_2S_3@NSC, and YS-Sb_2S_3@NSC electrodes at 1 A g^{-1}.

495.3, 423.2, 313, and 210 mA h g^{-1} at 0.05, 0.1, 0.2, 0.5, 1, 2, and 4 A g^{-1}, respectively. In contrast, as the current density increases to 0.2 A g^{-1} for bare Sb_2S_3 and 1 A g^{-1} for CS-Sb_2S_3@NSC, the specific capacities of these two control electrodes even decay completely. Moreover, the specific capacity of YS-Sb_2S_3@NSC can be fully restored when the current density recovers to 0.05 A g^{-1}, with a high reversible capacity of 614.86 mA h g^{-1} at the 100th cycle, which significantly surpasses the bare Sb_2S_3 (18.7 mA h g^{-1}) and CS-Sb_2S_3@NSC (447.58 mA h g^{-1}). As shown in Fig. 3(e), discharge-charge curves with similar shapes further confirm the superior rate capability of the YS-Sb_2S_3@NSC electrode, which is associated with the enhanced electrical conductivity provided by the carbon shell. The cycle stability of the three electrodes was investigated at 1 A g^{-1} as shown in Fig. 3(g) with the bare NSC electrode given in Fig. S10. After 1000 cycles, specific capacities of 255.66, 61.12, and 0.3 mA h g^{-1} can be obtained for YS-Sb_2S_3@NSC, CS-Sb_2S_3@NSC, and bare Sb_2S_3, respectively, which are highly related to their nanostructures. Impressively, the YS-Sb_2S_3@NSC electrode can maintain a high reversible capacity of 248.43 mA h g^{-1} even after 2000 cycles, with a slight capacity degradation of 0.01% per cycle compared to the 3rd cycle, which is superior to most of the reported Sb-based electrodes (Fig. 3f and Table S2) [17,19,21,31–38]. Based on the above results, it can be concluded that the carbon coating can effectively improve the reaction kinetics, thus boosting the rate performance. Nevertheless, considering the huge expansion stress of Sb_2S_3 and the associated structural destruction, carbon coating can only improve the cycle performance to a limited extent. Furthermore, by constructing buffer space to accommodate the large volume variation of Sb_2S_3, which could protect the carbon layers against breaking and cracking during cycling, thus the YS-Sb_2S_3@NSC electrode exhibits a super-stable cyclability.

3.3. Kinetics and quantitative analysis

The reaction kinetics of the Sb_2S_3-based electrodes were investigated via CV measurements at different scan rates, EIS, and GITT. As shown in Figs. S13 and S14, the characteristic peaks shift and weaken as the scan rate increases, indicating the more significant polarization and rapid capacity fading of the bare Sb_2S_3 electrode [19]. Instead, CV curves of the YS-Sb_2S_3@NSC electrode exhibit similar shapes (Fig. 4a), which reveal its slight polarization and excellent electrochemical reversibility and stability. According to the relationship between the peak current and the sweep rate (Eq. S2), the *b* values of YS-Sb_2S_3@NSC can be calculated. Since these values are between 0.76 and 0.89 (Fig. 4b), it can be inferred that the pseudocapacitive effect plays a significant role in electrochemical storage [39]. The ratio of capacitive contributions can be quantitatively distinguished following Eq. (S3). As depicted in Fig. 4(c), with the increase in scan rate, the ratio of capacitive contribution gets larger, demonstrating the improved surface-controlled behavior of the YS-Sb_2S_3@NSC electrodes at high rates. EIS was conducted to understand the K^+ diffusion kinetic at the pristine state, and the situation after different cycles (Fig. 4d and e, Figs. S15 and S16) and the fitted charge transfer resistance (R_{ct}) are presented in Fig. S16 and Table S3. Compared to the pristine state, the R_{ct} decreases sharply for both electrodes after the first cycle (Fig. 4d), representing the activation process [40]. Interestingly, in the subsequent cycles, the R_{ct} of YS-Sb_2S_3@NSC gradually decreases along with cycles, which can be ascribed to the improved

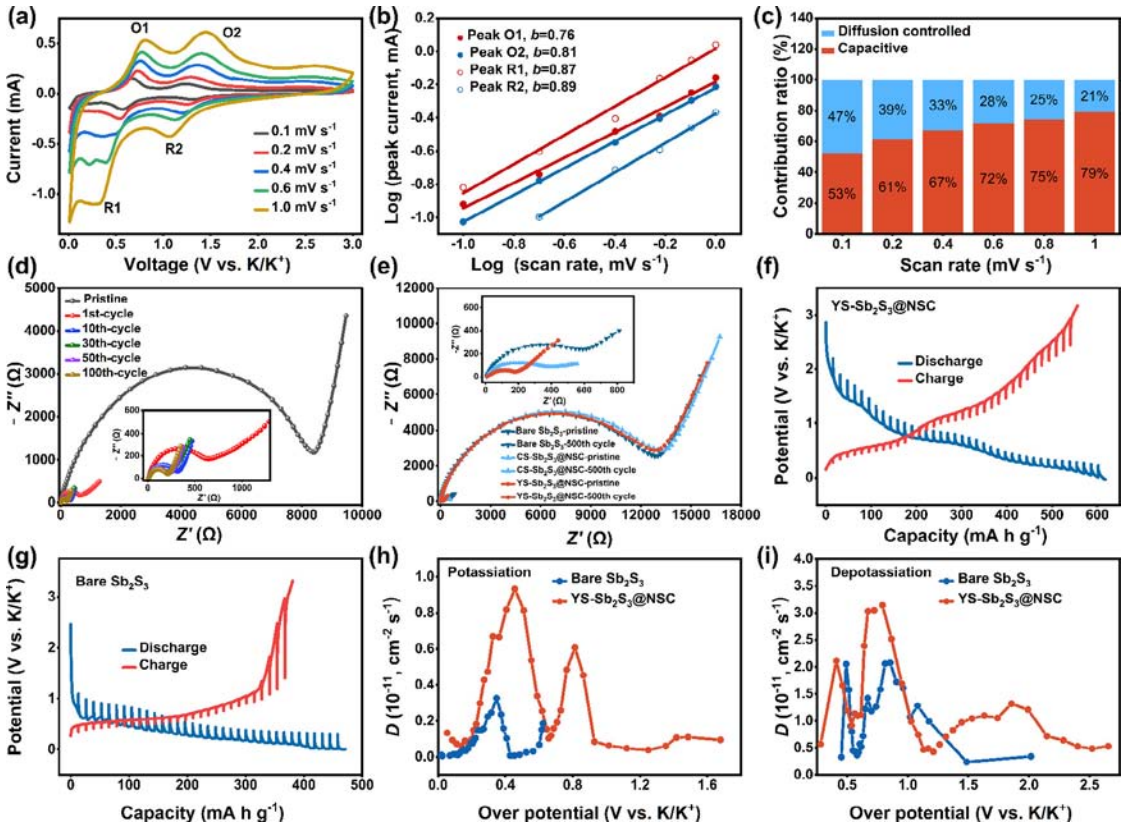

Fig. 4. (a) CV curves of YS-Sb_2S_3@NSC at different scan rates. (b) Log(*i*) vs. log (*v*) plots for different peaks in (a). (c) Capacitive contribution ratio at different scan rates and (d) EIS profiles at various cycles for the YS-Sb_2S_3@NSC electrodes. (e) Comparison of the EIS of three samples between pristine state and 500th cycles. (f, g) GITT potential profiles of YS-Sb_2S_3@NSC and bare Sb_2S_3. (h, i) Corresponding diffusion coefficients during potassiation and depotassiation.

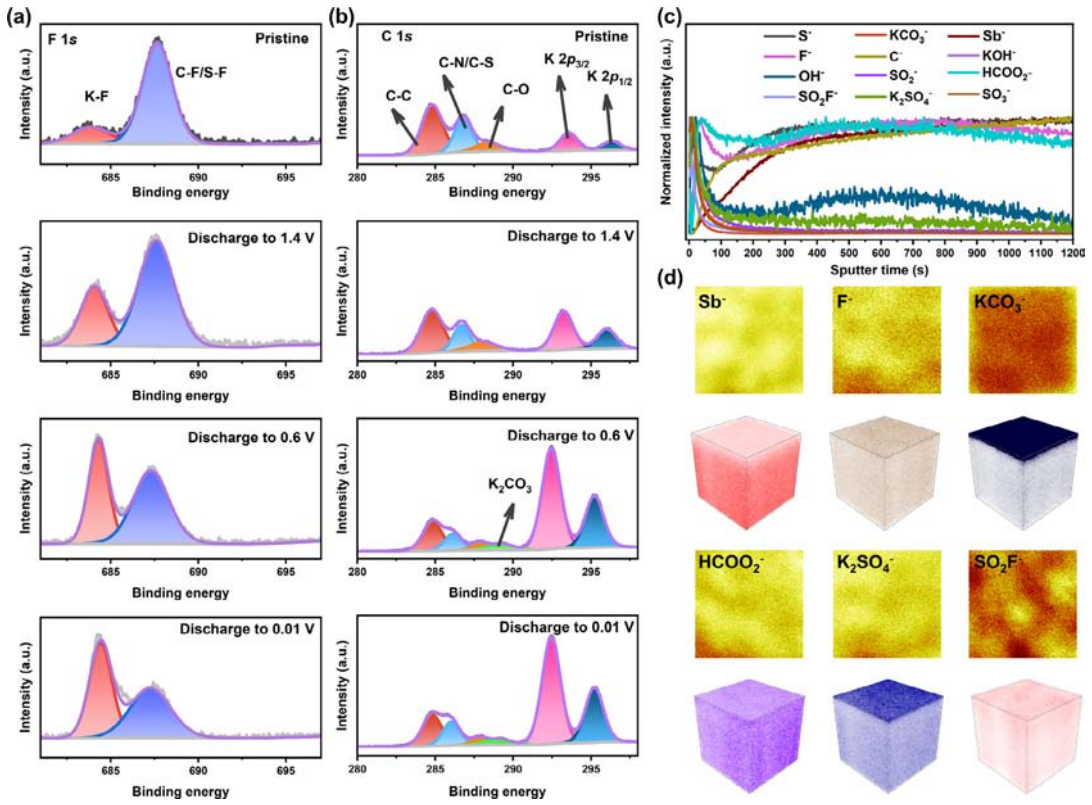

Fig. 5. XPS measurements of the YS-Sb_2S_3@NSC electrodes in DME at different discharge states for (a) the high-resolution F 1*s* XPS and (b) the high-resolution C 1*s* XPS. (c) Depth profile of various secondary ion species obtained by sputtering. (d) The 3D view images of the sputtered volume corresponding to the depth profiles in (c).

charge transfer dynamics during cycling. Moreover, Fig. 4(e) shows the EIS curves of the three samples at the pristine state and after 500 cycles at 4 A g^{-1}. The R_{ct} value of YS-Sb_2S_3@NSC after 500 cycles is significantly lower than that of other samples, which further confirms the enhanced electrochemical stability of YS-Sb_2S_3@NSC [41]. In addition, GITT was applied to explore the K-ions diffusion coefficient (D_K) of the three electrodes (Fig. S17). According to solving Fick's second law (Eqs. S4–S6), the D_K value can be calculated. Fig. 4(h and i) shows that YS-Sb_2S_3@NSC delivers a higher D_K value compared to bare Sb_2S_3 and CS-Sb_2S_3@NSC (Fig. S18) at most potentials, which is associated with its enhanced electronic conductivity after cooperating with carbon shells [42].

Ex situ XPS and TOF-SIMS measurements were performed to study the composition of the SEI films. The SEI formed in the KFSI-DME electrolyte was found to derive from the decomposition of KFSI salts [43]. And, the KFSI-derived SEI was mainly consisted of inorganic salt. As the discharge process progresses, F 1*s* spectra of ex situ XPS results (Fig. 5a) demonstrate that an inorganic-rich SEI formed on carbon-layer, with the increased intensity of K-F species. The SEI with high K-F content is capable of forming protective layer effectively to prevent the formation of new SEI, favoring for maintaining the stability of the charge transmission impedance [44]. As shown in Fig. 5(b), there is no signal peak of carbonate in the pristine state and discharge intermediate state (1.4 V). Apparently, it appears at 0.6 V, corresponding to the formation of SEI films from the decomposition of KFSI. Overall, the ex situ XPS results demonstrate the formation of inorganic-based and F-rich SEI films during the first discharge, benefiting for achieving enhanced charge transfer kinetics, and reducing the EIS (R_{ct}) after the first cycle [45–47]. In addition, the full-discharged electrode in 5 M KFSI electrolyte systems was examined by TOF-SIMS. As shown in Fig. 5(c and d), at the beginning of the sputter time, many ion fragments (F^-, OH^-, KCO_3^-, $HCOOK^-$, COO^-, KOH^-, SO_2^-, SO_3^-, K_2SO4^-, SO_2F^-) are detected near the surface region in the concen-

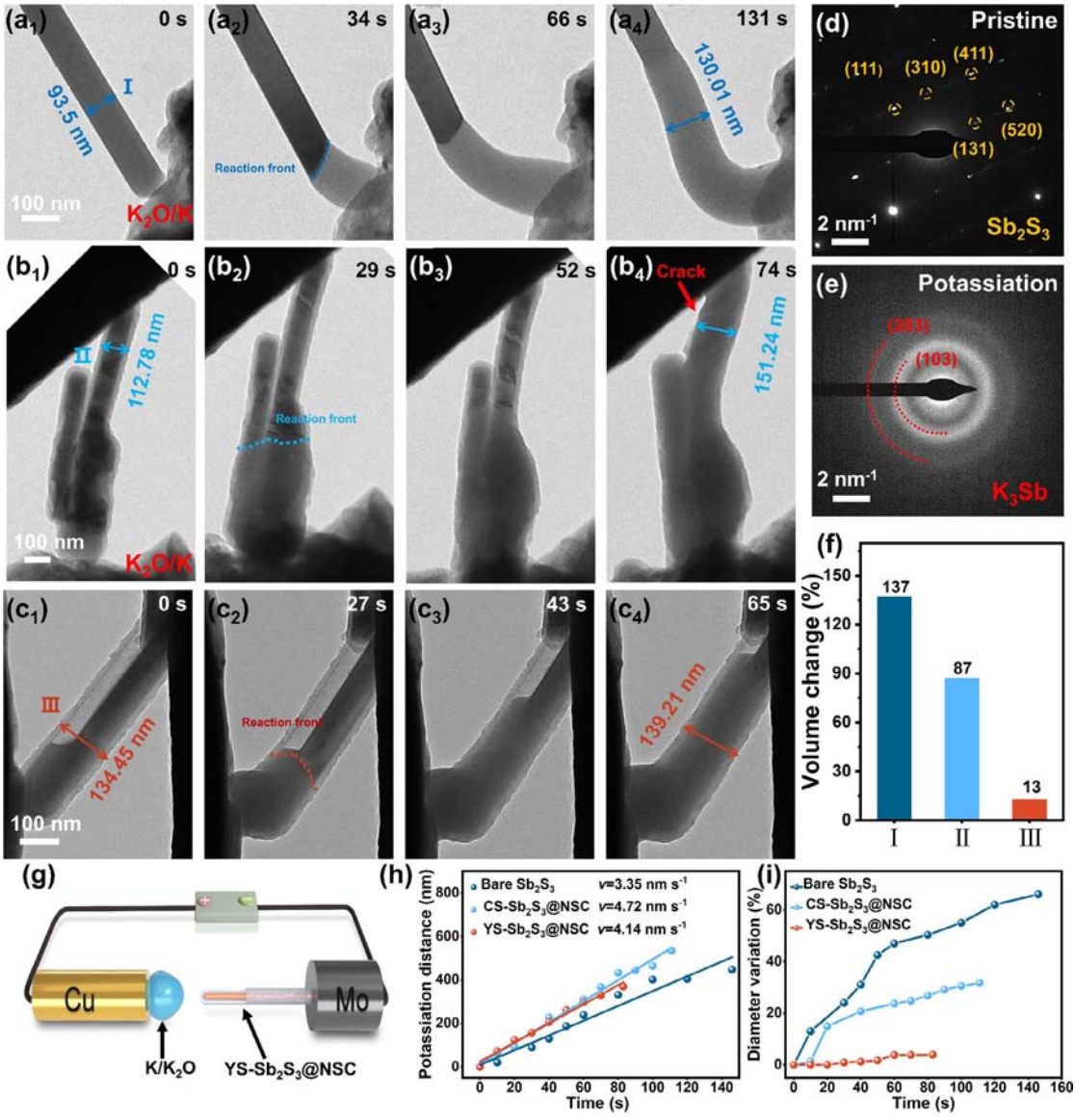

Fig. 6. Time-resolved TEM images of the morphological evolution for (a) bare Sb_2S_3, (b) CS-Sb_2S_3@NSC, and (c) YS-Sb_2S_3@NSC during the first potassiation. The SAED patterns of YS-Sb_2S_3@NSC in states of (d) pristine and (e) the first potassiation. (f) The volume change of the three samples after the first potassiation. (g) Schematic illustration of the in situ TEM device. (h) Propagation distances of the reaction fronts along with the three samples as functions of potassiation time. (i) Comparison of the expansion ratio of the three samples during potassiation.

trated electrolyte. With the sputter time increases, the intensity of C^-, S^- and Sb^- species increases accordingly, demonstrating the exposure of inner YS-Sb_2S_3@NSC. The signal intensity of F^- keeps a high level with the increase of time, indicating that an inorganic based, F-rich and evenly-distributed SEI is formed on the YS-Sb_2S_3@NSC electrode, corresponding to the XPS results. The formation of the F-rich solid electrolyte interface on YS-Sb_2S_3@NSC has demonstrated to be beneficial for reducing the solubility of inorganic substances in the electrolyte and stabilizing the interface and thus accounting for enhanced rate performance [48].

3.4. Insight into the origins of performance enhancement and K^+ storage mechanism

To investigate the electrochemically induced structural evolution and its effect on the performance of bare Sb_2S_3, CS-Sb_2S_3@NSC and YS-Sb_2S_3@NSC, in situ TEM studies on the live potassiation process was carried out as shown in Fig. 6 (captured from the Videos S1-S3). The solid-state nanobattery inside the TEM consists of a K metal counter electrode, a K_2O solid electrolyte, and an Sb_2S_3-based working electrode (Fig. 6g). A bias of +3 V would be applied on the K/K_2O electrode to induce potassiation of Sb_2S_3-based nanorodes. Fig. 6 (a–c) shows the time-resolved TEM images of different samples during the first potassiation process. For bare Sb_2S_3 (Fig. 6a), the potassiation process can be visualized by the propagation of K^+ along the nanorod accompanied by huge volume expansion, and a distinct reaction front can be observed at the boundary between the potassiated and unpotassiated parts (as indicated by mazarine dotted lines). The Sb_2S_3 nanorod gets swelled and curved during potassiation (Fig. 6a_{2-4}), suggesting expansion in both radial and axial directions. After the full potassiation (Fig. 6a_4), the average diameter variation of the nanorod reaches 39%, along with significant axial elongation, manifesting the huge structural change of Sb_2S_3 after K^+ insertion. To address this problem, surface carbon coating was introduced to suppress the volume expansion for CS-Sb_2S_3@NSC. As shown in Fig. 6(b), significant radial expansion occurs when K^+ diffuses along the nanorod, while the axial expansion is slight, which is different from bare Sb_2S_3. After fully potassiated (Fig. 6b_4), the diameter and length of CS-Sb_2S_3@NSC nanorod increased by ~32% and ~11%, respectively, lower than that of Sb_2S_3 in both radial and axial directions, which can be ascribed to the mechanical confinement of the surface carbon layer. However, apparent cracking of the carbon shell can also be observed at this state (Fig. 6b_4), which leads to the extrusion of partial active materials, demonstrating that the surface coating is not robust enough to withstand the enormous expansion stress of Sb_2S_3 fully. Impressively, benefiting from the internal buffer space, the YS-Sb_2S_3@NSC nanorod during potassiation shows excellent structural integrity without cracks in the carbon shell. Interestingly, after the full potassiation, the diameter of the nanorod only expands from 134 to 139 nm with no detectable axial expansion (Fig. 6c), which is much slighter than bare Sb_2S_3 and CS-Sb_2S_3@NSC. Note that the huge volume expansion of the encapsulated Sb_2S_3 still occurs in YS-Sb_2S_3@NSC. However, the cavity between the Sb_2S_3 and carbon layer could buffer this huge volume expansion and prevent the stress-induced damage to the protective shell, thus ensuring its robust mechanical stability. This stability can be seen intuitively by comparing the volume expansion ratio for different samples after the first potassiation, as depicted in Fig. 6(f). Moreover, Fig. 6(d and e) shows the corresponding SAED patterns before and after the first potassiation, revealing the formation of K_3Sb as the final K-Sb alloying product. According to the statistics, YS-Sb_2S_3@NSC exhibits a faster propagation speed than bare Sb_2S_3, as well as the lowest diameter variation ratio among three samples (Fig. 6h and i), thus ensuring its

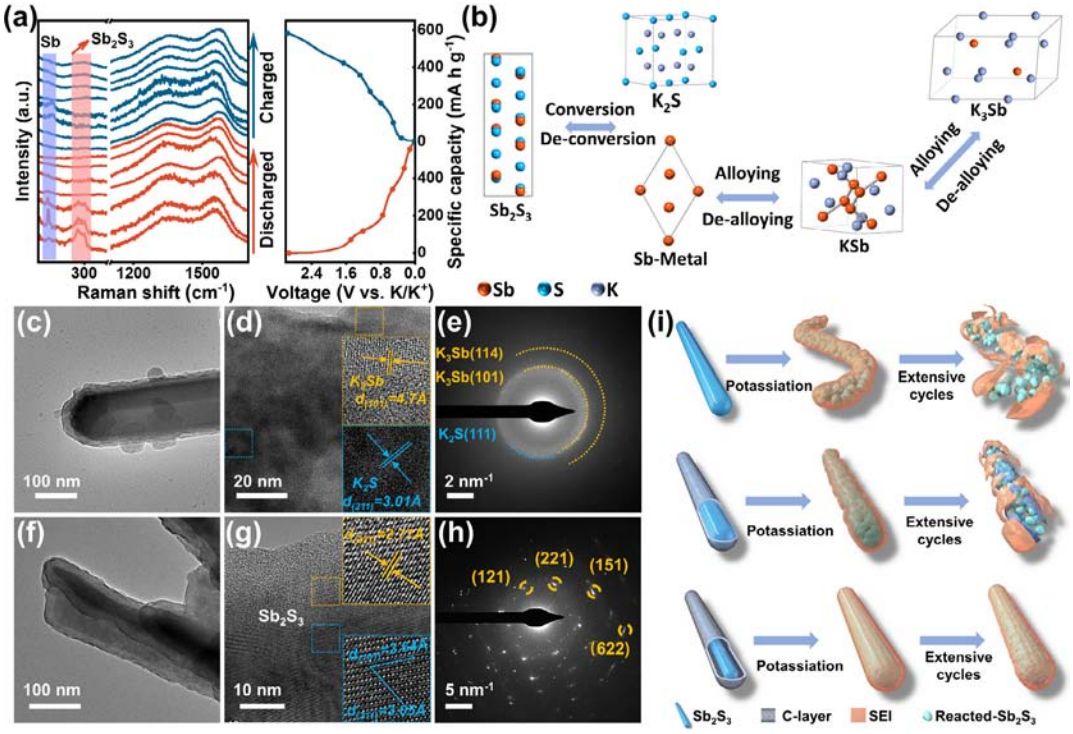

Fig. 7. (a) Operando Raman spectra and (b) schematic diagram of the potassium storage mechanism of the YS-Sb_2S_3@NSC electrode. TEM, HRTEM images, and the corresponding SAED pattern of YS-Sb_2S_3@NSC (c–e) after the full potassiation and (f–h) after the full depotassiation. (i) Schematic illustration of the morphology evolutions of bare Sb_2S_3, CS-Sb_2S_3@NSC, and YS-Sb_2S_3@NSC during cycling.

excellent rate capability and super-stable cycle performance as presented above.

To gain insight into the K^+ storage mechanism of the Sb_2S_3 anode, operando Raman spectra and ex situ TEM characterizations were performed upon potassiation/depotassiation. As shown in Fig. 7(a), in the pristine state, the peak at 269 cm^{-1} corresponds to the vibrations of pyramidal units Sb–S in Sb_2S_3. When the electrode discharges to 1.5 V, the characteristic peak of hexagonal Sb at 144 cm^{-1} appears, manifesting the occurrence of conversion reactions. After discharging to 0.5 V, all peaks completely vanish, representing the K-Sb alloying reactions. As shown in Fig. 7(d and e), both the HRTEM image and SAED pattern demonstrate the existence of K_3Sb and K_2S after discharging to 0.01 V, confirming that the final potassiated products of YS-Sb_2S_3@NSC are K_3Sb and K_2S, which is consistent well with previous reports [16]. During depotassaition, the peak of Sb first reappears at 0.59 V and then disappears at 1.08 V (Fig. 7a), corresponding to the dealloying reaction of K_xSb and the deconversion process, respectively. In particular, after the full depotassiation, the characteristic peak belonging to Sb_2S_3 can be observed, together with the crystal planes occurring in the HRTEM image and SAED pattern (Fig. 7g and h), which reveals the high reversibility of the YS-Sb_2S_3@NSC electrode. Based on the above results, the reaction mechanism of Sb_2S_3 during potassiation/depotassiation is described in Fig. 7(b). Moreover, the structural changes of the three electrodes after cycling were investigated through ex situ SEM/TEM observations (Figs. S19 and 20). The YS-Sb_2S_3@NSC electrode, after 100 cycles, exhibits a smooth surface without cracks or fractures, where the nanorods morphology is well maintained (Fig. S19a–c). In contrast, the bare Sb_2S_3 and CS-Sb2S3@NSC electrodes display a fragmented structure with obvious cracks after cycling, accompanied by the degradation of nanorods, leading to electrode failures. These results follow in situ TEM observations. According to the electron microscopy results from micro to macro scale, the morphology evolutions of bare Sb_2S_3, CS-Sb_2S_3@NSC, and YS-Sb_2S_3@NSC during cycling are illustrated in Fig. 7(i). Benefiting from the carbon shell cooperated with buffer space that effectively accommodates the enormous expansion stress of Sb_2S_3, YS-Sb_2S_3@NSC exhibits much more stable cycling performance than bare Sb_2S_3 and CS-Sb_2S_3@NSC, correlating with the above-mentioned electrochemical performance.

4. Conclusions

In summary, a yolk-shell structured Sb_2S_3 confined in N, S co-doped hollow carbon nanorod (YS-Sb_2S_3@NSC) has been successfully developed and further investigated as a high-capacity and long-life anode for PIBs. Through systematic in situ TEM studies on the live potassiation process, we have tracked the dynamic structural evaluations of different Sb_2S_3-carbon composites at a microscopic scale and then revealed the effects of carbon coating and buffer space on stabilizing Sb_2S_3 nanorods. Importantly, for YS-Sb_2S_3@NSC electrode, we have clearly observed that the cavity between the Sb_2S_3 core and carbon shell can effectively buffer the huge volume expansion of Sb_2S_3 without cracking the shell, while the N, S co-doped carbon shell facilitates the ionic/electronic transport, thus ensuring its robust structural stability and fast reaction kinetics. Accordingly, the YS-Sb_2S_3@NSC electrode delivers a super-stable cyclability of 248.43 mA h g^{-1} at 1 A g^{-1} over 2000 cycles and a high-rate performance of 210 mA h g^{-1} at 4 A g^{-1}, which outperforms the reference bare Sb_2S_3 and CS-Sb_2S_3@NSC anodes alongside most of the reported Sb-based anode materials. Further, supported by the results of operando Raman, and in situ/ex situ TEM observations coupled with ex situ XPS and TOF-SIMS measurements, the K^+ storage mechanism and origins of performance enhancement of YS-Sb_2S_3@NSC have been carefully uncovered. Our findings may provide valuable guidance for the rational design of high-performance and durable transition metal sulfides-based anode materials for advanced PIBs.

Declaration of competing interest

The authors declare that they have no known competing financial interests or personal relationships that could have appeared to influence the work reported in this paper.

Acknowledgments

B.X. and H.Z. contributed equally to this work. This work is supported by the National Natural Science Foundation of China (Grants Nos. 52072323 and 52122211), the "Double-First Class" Foundation of Materials and Intelligent Manufacturing Discipline of Xiamen University and the State Key Laboratory of Alternate Electrical Power System with Renewable Energy Sources (Grant No. LAPS22005)

Appendix A. Supplementary data

Supplementary data to this article can be found online at https://doi.org/10.1016/j.jechem.2022.09.050.

References

[1] J. Ge, L. Fan, A. Rao, J. Zhou, B. Lu, Nat. Sustain. 5 (2022) 225–234.
[2] L. Wang, B. Zhang, B. Wang, S. Zeng, M. Zhao, X. Sun, Y. Zhai, L. Xu, Angew. Chem. Int. Ed. 60 (2021) 15381–15389.
[3] H. Zhang, Y. Cheng, J. Sun, W. Ye, C. Ke, M. Cai, H. Gao, P. Wei, Q. Zhang, M.-S. Wang, Adv. Energy Mater. 12 (2022) 2201259.
[4] M. Cai, H. Zhang, Y. Zhang, B. Xiao, L. Wang, M. Li, Y. Wu, B. Sa, H. Liao, L. Zhang, S. Chen, D. Peng, M. Wang, Q. Zhang, Sci. Bull. 67 (2022) 933–945.
[5] L. Deng, J. Qu, X. Niu, J. Liu, Y. Zhu, Nat. Commun. 12 (2021) 2167.
[6] Y. Li, Q. Zhang, Y. Yuan, H. Liu, C. Yang, Z. Lin, J. Lu, Adv. Energy Mater. 10 (2020) 2000717.
[7] K. Xi, X. Min, J. Xiao, M. Fang, Z. Huang, Energy Environ. Sci. 14 (2021) 2186–2243.
[8] H. Zhang, Y. Cheng, Q. Zhang, W. Ye, M.-S. Wang, ACS Nano 15 (2021) 10107–10118.
[9] Z. Jian, W. Luo, X. Ji, J. Am. Chem. Soc. 137 (2015) 11566–11569.
[10] Y. Liu, Z. Tai, J. Zhang, W. Pang, Q. Zhang, H. Feng, K. Konstantinov, Z. Guo, H. Liu, Nat. Commun. 9 (2018) 3645.
[11] H. Gao, X. Guo, S. Wang, F. Zhang, H. Liu, G. Wang, EcoMat. 2 (2020) 12027.
[12] N. Wang, Z. Bai, Y. Qian, J. Yang, Adv. Mater. 28 (2016) 4126–4133.
[13] Z. Liu, X. Yu, X. Lou, U. Paik, Energy Environ. Sci. 9 (2016) 2314–2318.
[14] X. Fu, C. Shang, G. Zhou, X. Wang, J. Mater. Chem. A 9 (2021) 24963–24970.
[15] D. Yu, P. Prikhodchenko, C. Mason, S. Batabyal, J. Gun, S. Sladkevich, A. Medvedev, O. Lev, Nat. Commun. 4 (2013) 2922.
[16] Y. Cheng, Z. Yao, Q. Zhang, J. Chen, W. Ye, S. Zhou, H. Liu, M.-S. Wang, Adv. Funct. Mater. 52 (2020) 2005417.
[17] H. Liu, Y. He, K. Cao, S. Wang, Y. Jiang, X. Liu, K. Huang, Q. Jing, L. Jiao, Small 17 (2021) 2008133.
[18] J. Wang, L. Fan, Z. Liu, S. Chen, Q. Zhang, L. Wang, H. Yang, X. Yu, B. Lu, ACS Nano 13 (2019) 3703–3713.
[19] S. Chong, S. Qiao, X. Wei, T. Li, L. Yuan, S. Dong, W. Huang, iScience 24 (2021).
[20] V. Lakshmi, A. Mikhaylov, A. Medvedev, C. Zhang, T. Ramireddy, M. Rahman, P. Cizek, D. Golberg, Y. Chen, O. Lev, J. Mater. Chem. A 8 (2020) 11424–11434.
[21] T. Wang, D. Shen, H. Liu, H. Chen, Q. Liu, B. Lu, ACS Appl. Mater. Interfaces 12 (2020) 57907–57915.
[22] K. Li, X. Liu, Y. Qin, Z. Zhao, Y. Xu, Y. Yi, H. Guan, Y. Fu, P. Liu, D. Li, Chem. Eng. J. 414 (2021).
[23] H. Ye, Z. Wang, J. Yan, Z. Wang, J. Chen, Q. Dai, Y. Su, B. Guo, H. Li, L. Geng, C. Du, J. Wang, Y. Tang, L. Zhang, L. Zhu, J. Huang, Adv. Funct. Mater. (2022) 2204231, https://doi.org/10.1002/adfm.202204231.
[24] Y. Wu, J. Zheng, Y. Tong, X. Liu, Y. Sun, L. Niu, H. Li, ACS Appl. Mater. Interfaces 13 (2021) 51066–51077.
[25] H. Zhang, W. Li, J. Pan, Z. Sun, B. Xiao, W. Ye, C. Ke, H. Gao, Y. Cheng, Q. Zhang, M.-S. Wang, J. Energy Chem. 73 (2022) 533–541.
[26] L. Cao, X. Gao, B. Zhang, X. Ou, J. Zhang, W.-B. Luo, ACS Nano 14 (2020) 3610–3620.
[27] Z. Liu, H. Sun, X. Wang, Z.-Y. Gu, C. Xu, H. Li, G. Zhang, Y. He, X.-L. Wu, Energy Storage Mater. 48 (2022) 90–100.
[28] W. Zhan, M. Zhu, J. Lan, H. Wang, H. Yuan, X. Yang, G. Sui, Chem. Eng. J. 408 (2021).
[29] S. Yao, J. Cui, Y. Deng, W.G. Chong, J. Wu, M. Ihsan-Ul-Haq, Y.-W. Mai, J.-K. Kim, Energy Storage Mater. 20 (2019) 36–45.

[30] Y. Shi, D. Zhou, T. Wu, Z. Xiao, ACS Appl. Mater. Interfaces 14 (2022) 16379–16385.
[31] Y. Zhao, J. Zhu, S. Ong, Q. Yao, X. Shi, K. Hou, Z.J. Xu, L. Guan, Adv. Energy Mater. 8 (2018) 1802565.
[32] W. Luo, F. Li, W. Zhang, K. Han, J.-J. Gaumet, H.-E. Schaefer, L. Mai, Nano Res. 12 (2019) 1025–1031.
[33] X. Li, H. Liang, X. Liu, R. Sun, Z. Qin, H. Fan, Y. Zhang, Chem. Eng. J. 425 (2021).
[34] Y. Zhao, X. Shi, S. Ong, Q. Yao, B. Chen, K. Hou, C. Liu, Z. Xu, L. Guan, ACS Nano 14 (2020) 4463–4474.
[35] H. Wang, X. Wu, X. Qi, W. Zhao, Z. Ju, Mater. Res. Bull. 103 (2018) 32–37.
[36] Q. Liu, L. Fan, R. Ma, S. Chen, X. Yu, H. Yang, Y. Xie, X. Han, B. Lu, Chem. Commun. 54 (2018) 11773–11776.
[37] X.-D. He, Z.-H. Liu, J.-Y. Liao, X. Ding, Q. Hu, L.-N. Xiao, S. Wang, C.-H. Chen, J. Mater. Chem. A 7 (2019) 9629–9637.
[38] J. Han, K. Zhu, P. Liu, Y. Si, Y. Chai, L. Jiao, J. Mater. Chem. A 7 (2019) 25268–25273.
[39] H. Sun, Y. Zhang, X. Xu, J. Zhou, F. Yang, H. Li, H. Chen, Y. Chen, Z. Liu, Z. Qiu, D. Wang, L. Ma, J. Wang, Q. Zeng, Z. Peng, J. Energy Chem. 61 (2021) 416–424.
[40] K.-T. Chen, H.-Y. Tuan, ACS Nano 14 (2020) 11648–11661.
[41] P. Ge, H. Hou, S. Li, L. Yang, X. Ji, Adv. Funct. Mater. 28 (2018) 1801765.
[42] H. Guan, H. He, T. Zeng, C. Zhang, J. Energy Chem. 63 (2021) 633–641.
[43] H.J. Kim, J.H. Jo, J.U. Choi, N. Voronina, D. Ahn, T.-Y. Jeon, H. Yashiro, Y. Aniskevich, G. Ragoisha, E. Streltsov, S.-T. Myung, Energy Storage Mater. 40 (2021) 197–208.
[44] Z. Wu, J. Zou, S. Shabanian, K. Golovin, J. Liu, Chem. Eng. J. 427 (2022).
[45] H. Wang, D. Zhai, F. Kang, Energy Environ. Sci 13 (2020) 4583–4608.
[46] L. Fan, K. Lin, J. Wang, R. Ma, B. Lu, Adv. Mater 30 (2018) 1800804.
[47] H. Wang, D. Yu, X. Wang, Z. Niu, M. Chen, L. Cheng, W. Zhou, L. Guo, Angew. Chem. 131 (2019) 16603–16607.
[48] S. Zhao, Z. Liu, G. Xie, X. Guo, Z. Guo, F. Song, et al., Angew. Chem. Int. Ed. 60 (2021) 26246–26253.